Journal of Power Sources 246 (2014) 68–73

Contents lists available at SciVerse ScienceDirect

Journal of Power Sources

journal homepage: www.elsevier.com/locate/jpowsour

Synthesis of MnO_2–chitosan nanocomposite by one-step electrodeposition for electrochemical energy storage application

Sameh Hassan [a], Masaaki Suzuki [b], Ahmed Abd El-Moneim [c,*,1]

[a] Energy Resources and Environmental Engineering Department, Egypt–Japan University of Science and Technology, New Borg El Arab City, Alexandria 21934, Egypt

[b] Department of Chemical Engineering, Tokyo Institute of Technology, 2-12-1 O-Okayama, Meguro-ku, Tokyo 152-8552, Japan

[c] Material Science and Engineering Department, Egypt–Japan University of Science and Technology, New Borg El Arab City, Alexandria 21934, Egypt

HIGHLIGHTS

- Chitosan provides a mean for assembling manganese dioxide nanoparticles into macro-scale components.
- Chitosan promotes ions and electrons transport inside the matrix of manganese dioxide film.
- Manganese dioxide–chitosan composite presents high specific capacitance, long cycle life and superior rate capability.

ARTICLE INFO

Article history:
Received 24 February 2013
Received in revised form
2 June 2013
Accepted 14 June 2013
Available online 14 July 2013

Keywords:
Manganese dioxide
Chitosan
Cathodic deposition
Transmission electron microscopy

ABSTRACT

MnO_2–chitosan hybrid nanocomposite films with low and high chitosan's molecular weights are synthesized by one-step cathodic electrodeposition on nickel foam substrate for electrochemical capacitors (ECs) application. The films have been characterized using scanning electron microscopy (SEM), transmission electron microscopy (TEM), fourier transform infrared (FTIR) spectroscopy, cyclic voltammetry, galvanostatic charge–discharge, and electrochemical impedance spectroscopy. The MnO_2–chitosan hybrid nanocomposite films show better specific capacitance and rate capability than chitosan-free MnO_2 film. For the MnO_2–chitosan composite films, the highest specific capacitance is 424 F g^{-1} obtained at a current density of 1 mA cm^{-2}. The deposited film retains a very stable capacitance over 400 cycles by charging and discharging at 3 mA cm^{-2}, and only 3% capacity loss is observed. The presence of chitosan promotes both ion and electron transport in the matrix of MnO_2. Besides, it allows the formation of porous and crack-free deposited films. A deposition mechanism for MnO_2–chitosan hybrid nanocomposite films is proposed.

1. Introduction

Recently, the electrochemical energy storage systems such as rechargeable batteries and electrochemical capacitors (ECs) are receiving an increased consideration [1–10]. These noticeable attentions are due to the requirements of renewable energy production from sun and wind which generally have on-peak and off-peak load variations. Also due to the development of electric vehicles (EVs) or hybrid electric vehicles (HEVs) with low CO_2 emissions, they have a driving range of 150–200 miles before charging is required. ECs, with a combination of high power and reasonably high energy density, are a versatile solution to a variety of emerging energy applications.

So far, manganese oxides have attracted significant interest as active electrode materials for electrochemical processes, particularly ECs [10–24]. These oxides are characterized by reasonable specific capacitance, low-cost, abundance and environmentally friendly nature.

In general, hydrated manganese oxides exhibit specific capacitances within the 100–200 F g^{-1} range in aqueous solutions. Poor electrical conductivity ($\sim 10^5$ Ω cm) has been reported for micrometer-thick birnessite-type MnO_2 [24,25]. The specific capacitance and power characteristics of MnO_2 electrodes are ultimately limited by the high charge-transfer resistance. In addition to their poor electrical conductivity, another important issue is the electrochemical

* Corresponding author. Tel.: +20 1281229082; fax: +20 34599520.
E-mail addresses: ahmed.abdelmoneim@ejust.edu.eg, oneim99@yahoo.com (A.A. El-Moneim).

[1] On leave from Physical Chemistry Department, National Research Centre, Cairo, Egypt.

0378-7753/$ – see front matter © 2013 Elsevier B.V. All rights reserved.
http://dx.doi.org/10.1016/j.jpowsour.2013.06.085

cyclability of MnO_2 electrodes. Active material dissolution during electrochemical cycling has been well recognized in some investigations, which accounts for the major capacitance loss of the MnO_2 electrodes. Mechanical issues, such as low structural stability and flexibility, also exist in MnO_2 electrodes resulting in degraded long-term electrochemical cycle life [25].

An important consideration for alleviating the poor electronic conductivity, chemical and mechanical stabilities, and flexibility of MnO_2 electrodes is to tailor the electrode architecture via applying an ultrathin layer of MnO_2 on the surface of a porous, high surface area and electronically conducting structure to shorten the electron transport distance and obtain molecular level hybrid features. This can produce a good electrochemical performance without sacrificing the mass-loading of the MnO_2 phase. The porous architectures can be carbon nanofoams, template mesoporous carbon, nanotube assemblies and conductive polymers [12,25].

Recently, the aminopolysaccharide chitosan (CH), Fig. 1, emerges as an important polymeric material for soft matter fabrication; because this biopolymer possesses a set of physicochemical properties that uniquely equips it for hierarchical assembly of nanoscale components over a range of length scales. The number of glucosamine repeating unit (molecular weight), crystallinity and degree of deacetylation are parameters significantly affects the properties of CH.

The potential of CH as a length scale interconnects discussed in detail by Payne et al. [26] and illustrated in Fig. 2. As indicated in Fig. 2, CH provides sites for connecting nano-scale components (10^0–10^1 nm) along its carbon linear backbone (10^1–10^3 nm). Assembly at larger length scales occurs through chitosan's stimuli-responsive film/gel-forming properties that enable this polysaccharide to self-organize at the micro-scale (10^3 nm). Importantly, CH films and gels can be induced to form in response to localized electrical stimuli. Thus, chitosan offers properties both to connect length- and nano-scale components to electronic devices [26]. Finally, chitosan's metal binding properties [27–29] allow connections through chelation mechanisms [30–32].

Thus a composite electrode construction which incorporates nanoscopic MnO_2 particles on a long linear backbone of CH is thought as an ideal approach to optimize the electronic conductivity, chemical and mechanical stabilities, and flexibility of MnO_2 film for supercapacitor applications.

This effort has been carried out to build up hierarchical assembly connecting nanoscopic MnO_2 particles into macro-scale structure of CH via electrochemical deposition for supercapacitor application. Particular attention is given to elucidate the effect of chitosan's molecular weight on the capacitive behavior and cyclic stability of electrodeposited MnO_2 film.

2. Experimental

Two CH-raw materials with molecular weights of 300,000 (high) and 25,000 (low) KDa and degree of deacetylation (DA) higher than 85% were used in the deposition process of MnO_2–CH thin films. All films were cathodically deposited, at −0.1 V Ag/AgCl

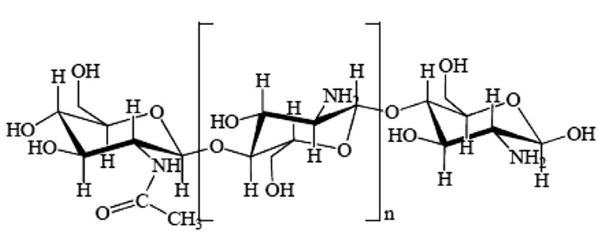

Fig. 1. Chemical structure of chitosan with its glucosamine repeating unit.

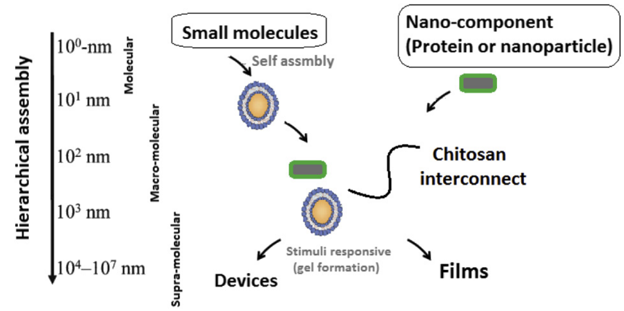

Fig. 2. Chitosan is a length-scale interconnect for hierarchical assembly.

(KCl saturated), on nickel foam substrate from 0.02 M $KMnO_4$ solution without and with 0.2 g l^{-1} chitosan which is pre-dissolved in 1% acetic acid solution. The mass of the deposited films was controlled by adjusting the total charge passed through the electrode during deposition process and confirmed by six digits microbalance. The estimated mass density of the deposited films was about 0.15 mg cm^{-2}.

The deposited films were observed using scanning electron microscope (Hitachi S-4500), transmission electron microscopy (JEOL JEM-2010F) and analyzed by FTIR spectrophotometer (Perkin Elmer–Spectrum BX II).

The cyclic voltammetry (CV), galvanostatic charge–discharge and electrochemical impedance spectroscopy (EIS) studies had been carried out in 0.5 M Na_2SO_4 electrolyte using VersaSTAT4 potentiostat/galvanostat electrochemical system. The electrochemical measurements had been conducted using a three-electrode system with platinum rod as a counter electrode and Ag/AgCl (KCl saturated) as a reference electrode. The EIS measurements were performed in the frequency range of 0.1 Hz–100 kHz.

The CV studies were performed within a range of 0–0.9 V versus Ag/AgCl (KCl saturated) at scan rates of 10–90 mV s^{-1}. The voltammetry specific capacitance (SC) was calculated as in equation (1) by using half the integrated area of the CV curve to obtain the charge (Q), and subsequently dividing the charge by the mass of the electrode (m) and the width of the potential window (ΔV):

$$SC = \frac{Q}{m \cdot \Delta V} \tag{1}$$

Galvanostatic charge/discharge cycling in the potential range of 0–1.0 V was performed at a constant current density in the range of 1–5 mA cm^{-2}. The obtained charge/discharge curves were used to calculate the discharge SC using equation (2)

$$SC = \frac{I}{(\mathrm{d}V/\mathrm{d}t)m} \tag{2}$$

Where dV/dt is the slope of the linear discharge curve and I is the current. The cycle life test was performed at current density of 3 mA cm^{-2} for 400 cycles. The SC was calculated according to the mass of MnO_2 film.

3. Results and discussion

3.1. Morphology and structure

Fig. 3 shows SEM different images of CH-free MnO_2 film (a) and MnO_2-CH films with low (b) and high (c) chitosan's M_w. As seen, the image of CH-free MnO_2 film (a) shows smooth film with continuous cracks. The film cracking can be attributed to drying shrinkage. It is

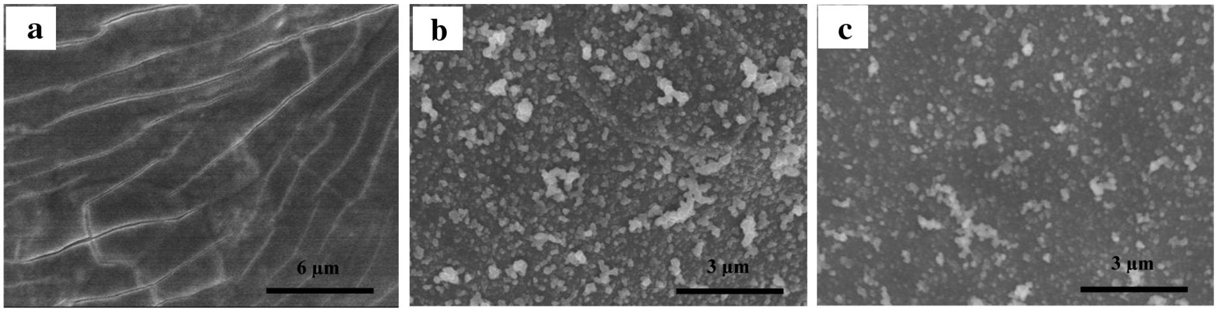

Fig. 3. SEM micrographs of CH-free MnO_2 film (a) and MnO_2–CH films with low (b) and high (c) chitosan's M_w.

suggested that the deposition of MnO_2 film requires the use of binders which can prevent film cracking. SEM investigations of the MnO_2–CH films, (b) and (c), reveals the deposition of crack-free films with coarse particle aggregates in the form of nanopellets. The nanopellets of the deposited film with low chitosan's M_w (b) are coarser than that with high chitosan's M_w (c).

Hence, the use of CH with its inherent binding properties allowed the formation of cracks-free films. Besides, chitosan's M_w is crucial in controlling the morphology of these films.

Fig. 4 depicts TEM images for CH-free MnO_2 (a) and MnO_2–CH (low M_w) (b) films. The images clearly show small and large dark spots of MnO_2 nano-domains which are dispersible throughout a porous network structure of CH (b). The increased porosity of the film containing CH can also result in preventing cracking due to crack-tip blunting mechanism [33].

According to HRTEM images shown in Fig. 5(a)–(c), overlapping crystalline lattice planes of the MnO_2 polymorph birnessite are clearly visible in the image of CH-free MnO_2 film, Fig. 5(a), and tend to diminish with the addition of CH as shown in Fig. 5(b) and (c). Specifically, MnO_2–CH (high M_w) film, Fig. 5(b), is amorphous and contains a small amount of a birnessite phase, while MnO_2–CH (low M_w) film, Fig. 5(c), is mainly amorphous. The formation of porous amorphous phase-based materials is generally feasible for supercapacitor and sensing applications due to the large accessible surface area and easy penetration of ions through the bulk of active materials.

3.2. FTIR spectroscopy analysis

In order to identify the exact location of the CH and oxide within the deposited MnO_2–CH composite films, FTIR spectroscopy analysis was carried out. Overlay FTIR spectra of raw chitosan with high M_w (a), CH-free MnO_2 film (b) and MnO_2–CH film with high chitosan's M_w (c) are shown in Fig. 6. It's clearly seen that the wider IR band at 3200–3500 cm^{-1} corresponds to –NH/OH stretching vibration modes in CH-raw material (a) [34,35] is found to be sharper and shifted to higher wave number in the spectrum of MnO_2–CH film (c). It appears that hydroxyl group and/or primary amines bind with MnO_2 nanoparticles via electrostatic interactions including weak *Van der Waal* forces and hydrogen bonding. Also, the peak position of IR band related to the coupling mode between Mn–O stretching modes of tetrahedral and octahedral sites [36–38] is shifted from 574 cm^{-1} in the IR spectrum of the MnO_2 deposited film (b) to 528 cm^{-1} in the IR spectrum of MnO_2–CH deposited film (c). This reflects a degree of distortion in the crystal structure of MnO_2, due to the formation of a complex between surfaces MnO_2 nanoparticles and CH matrix, and indicating the formation of CH–MnO_2 hybrid nanocomposite films [38].

3.3. Deposition mechanism

The results of FTIR analysis and, TEM and SEM characterization indicate the formation of porous MnO_2–CH hybrid nanocomposite films. The deposition mechanism of these films can be described as follows:

Nanoscopic MnO_2 film can be obtained by cathodic reduction of MnO_4^- species from $KMnO_4$ solution, using the following reaction:

$$MnO_4^- + 2H_2O + 3e^- \rightarrow MnO_2 + 4OH^- \quad (3)$$

Chitosan is soluble in water only when protonated in acidic solutions. At low pH, chitosan becomes a cationic polyelectrolyte [20]:

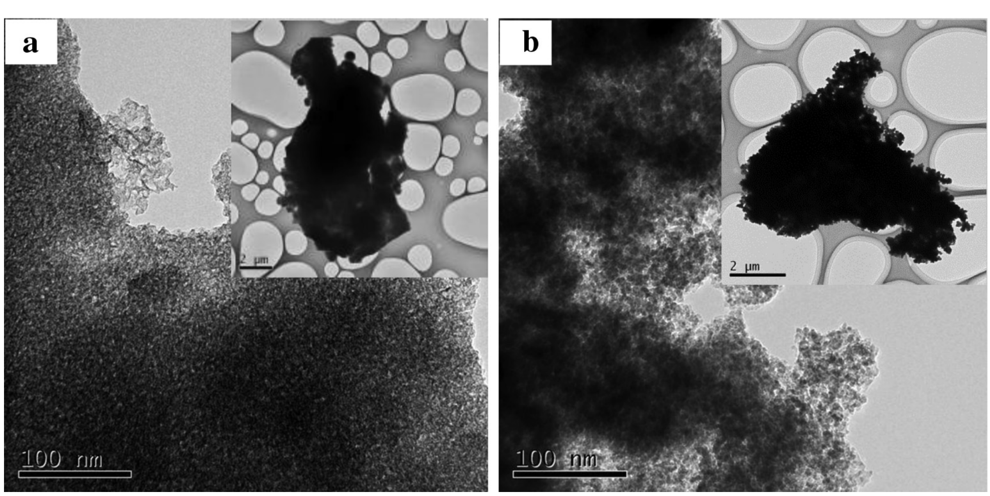

Fig. 4. TEM images of MnO_2 film (a) and MnO_2–CH film with low chitosan's M_w (b).

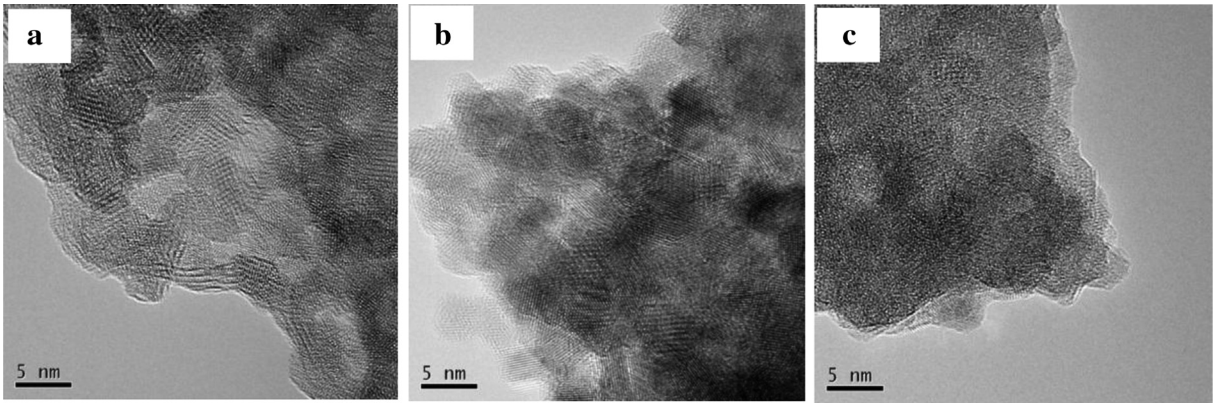

Fig. 5. HRTEM images of CH-free MnO_2 film (a) and MnO_2–CH films with high (b) and low (c) chitosan's M_w.

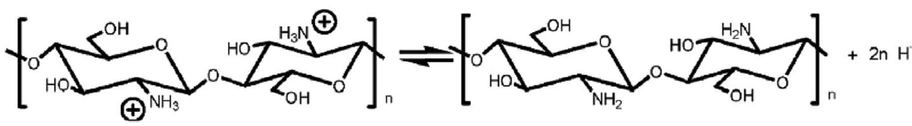

Under the action of an electric field, the charged chitosan molecules move toward the cathode surface.

$$2H_2O + 2e^- \rightarrow H_2 + 2OH^- \quad (4)$$

At the cathode, the reduction of water (2) and MnO_4^- species causes the local pH increases based on the reactions (3) and (4):

$$CH - NH_3^+ + OH^- \rightarrow Chit - NH_2(CH) + H_2O \quad (5)$$

Then, the chitosan loses its charge and forms insoluble species that co-deposited with MnO_2 during the electro-migration and diffusion MnO_4^- species toward the cathode surface.

During the course of the co-deposition process of CH with MnO_2, the hydroxyl group and/or primary amines (atomic length scale) of glucosamine repeating units (molecular length scale) of CH provide sites to connect amorphous MnO_2 nanoparticles to the polysaccharide backbone (macromolecular length scale). Connections to the backbone are formed by exploiting the electrostatic, including weak *Van der Waal* forces and hydrogen bonding, or metal-binding capabilities of glucosamine residues.

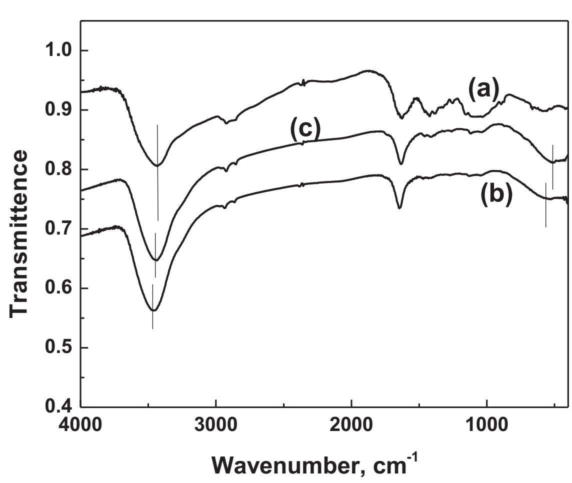

Fig. 6. FTIR spectra for CH-raw material with high M_w (a), CH-free MnO_2 film (b) and MnO_2–CH film with high chitosan's M_w (c).

In brief, aminopolysaccharide chitosan serves as a length-scale interconnect for porous hierarchical assembly of amorphous MnO_2 nanoparticles into micro-scale systems. Indeed, such a structure will be highly beneficial for harvesting the capacitance of the oxide as will be seen in the coming sections.

3.4. Capacitive behavior

3.4.1. Cyclic voltammetry

Fig. 7 shows the CV comparisons between CH-free MnO_2 (a) and MnO_2–CH hybrid nanocomposite films with low (b) and high (c) chitosan's M_w in 0.5 M Na_2SO_4 electrolyte at a scan rate of 90 mV s^{-1}. The inset of Fig. 7 presents the variation of the voltammetry SC of the films with scan rate.

The CV curves in Fig. 7 show rectangular shape indicative of highly capacitive nature with good ion response for all films. The cyclic voltammetry SC value (inset of Fig. 7) typically decreases as the scan rate increases and the highest SC values obtained for CH-free MnO_2, MnO_2–CH (high M_w) and MnO_2–CH (low M_w) films at a

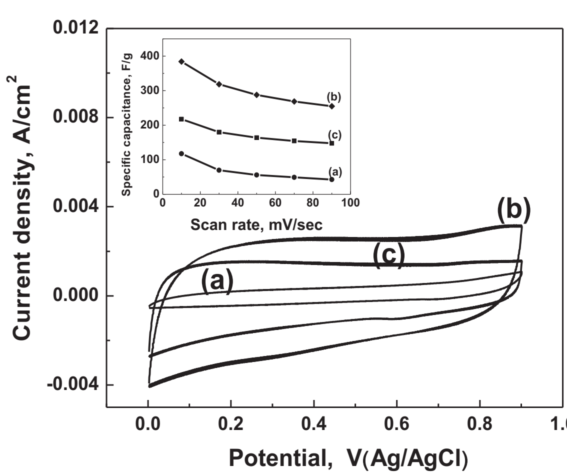

Fig. 7. CVs for CH-free MnO_2 film (a) and MnO_2–CH hybrid nanocomposite films with low (b) and high (c) chitosan's M_w in 0.5 M Na_2SO_4 electrolyte at a scan rate of 90 mV s^{-1}. The inset presents the variation of SC of the films with scan rate.

scan rate of 10 mV s^{-1} are 117, 218, and 384 F g^{-1}, respectively. Hence, MnO_2–CH films deliver higher SC than CH-free MnO_2 film, and that with low chitosan's M_w is the highest.

3.4.2. Galvanostatic charge–discharge characteristics

To further clarify the effect of CH on the capacitive behavior and rate capability of all MnO_2-based films, the charge and discharge behavior was examined by chronopotentiometry.

Fig. 8 shows charge–discharge profiles for CH-free MnO_2 film (a) and MnO_2–CH nanocomposite films with low (b) and high (c) chitosan's M_w at current density of 1.0 mA cm^{-2}. The inset presents the variation of the discharge SC for the examined films with the discharge current density.

In principle, the discharge profile of any oxide film with capacitive characteristics is basically consisted of three parts: a resistive component from sudden voltage drop (IR drop) due to the internal resistance of the deposited film, the capacitance component related to the voltage change due to ion separation in the double layer region at the electrode interface, and finally faradaic component in the longer time region due to charge transfer reaction of the film.

As can be seen in Fig. 8, the IR drops for MnO_2–CH nanocomposite films, particularly that with low chitosan's M_w (b), are much less as compared with CH-free MnO_2 film, indicating that the composite films have the lower internal resistance, ultimately lower charge transfer resistance, than CH-free MnO_2 film.

Moreover, the MnO_2–CH nanocomposite films, particularly that with low chitosan's M_w (b), show longer discharge times, which is equivalent to higher specific capacitance, than CH-free MnO_2 film. Meanwhile, the inset of Fig. 8, clearly shows that the discharge SC insignificantly decreases by applying high discharge current density, and the highest SC values for MnO_2, MnO_2–CH (high M_w) and MnO_2–CH (low M_w) films are 100, 225 and 424 F g^{-1}, respectively. This indicates that MnO_2–CH nanocomposite films not only show higher SC but also better capability rate of charge–discharge than CH-free MnO_2 film.

3.4.3. Electrochemical impedance spectroscopy studies

Electrochemical impedance measurements were carried out in order to quantify the conductive and diffusive behavior of the newly developed composite films.

Fig. 9 shows Nyquist plots for CH-free MnO_2 film (a) and MnO_2–CH nanocomposite films with low (b) and high (c) chitosan's M_w. The inset represents the high-frequency region of Fig. 9.

In general, the impedance spectra of films used in supercapacitor application are composed of a high-frequency arc region followed by a low-frequency line. The arc in the high-frequency region corresponds to the charge transfer resistance (R_{ct}) caused by the charge transfer process (Faradaic reactions) and double layer charging on the electrode surface. The magnitude of the R_{ct} can typically be derived from diameter of the arc [39–41]. The line at lower frequency region is a result of ion diffusion/transport (Warburg resistance) through the pores of the deposited films [42].

The EIS spectra in Fig. 9 are typical spectra of porous films. The obtained R_{ct} values for CH-free MnO_2, MnO_2–CH with high chitosan's M_w and MnO_2–CH with low chitosan's M_w films are about 294, 0.36, and 0.33 Ω, respectively. The sharp drop in the R_{ct} value with the presence of CH is consistent with the chronopotentiometry results presented in Fig. 8. It's also worth noted that the slope of the Nyquist plot in the low-frequency region is increased with CH addition, indicative of the decreasing Warburg resistance (or diffusion resistance). These results are in good agreement with the SEM, TEM, CV and galvanostatic charge/discharge results, verifying that the presence of CH leads to smaller charge transfer and diffusion resistances. In other words, presence of CH developed more ionic and electronic conductive network in the MnO_2–CH nanocomposite films.

3.4.4. Galvanostatic charge–discharge cyclic stability

The electrochemical stability of the MnO_2–CH with high chitosan's M_w and MnO_2–CH with low chitosan's M_w films was examined by charging and discharging at 3 mA cm^{-2} and the results are presented in Fig. 10. It's clearly seen in Fig. 10 and its inset that the MnO_2–CH with high chitosan's M_w retained a very stable capacitance over 400 cycles, as the capacity loss is only 3%, indicative of long-term electrochemical cycling stability.

In accordance with the previous, we have subtly realized the codeposition of CH during the growth of nanoscopic MnO_2 through a simple and appropriate synthesis process (one-step electrodeposition), preparing a composite electrode with hierarchical porous structure and better conductivity. The use of CH with its inherent binding properties allowed the formation of adherent and crack-free films. Furthermore, the less blocky structure of low chitosan's M_w efficiently enhances the formation of amorphous structure, which in turn promotes the capacitive behavior of MnO_2 film via increasing both ions and electrons transports inside it's the matrix. Hence, MnO_2–CH hybrid nanocomposite with low chitosan's M_w presents high SC and superior rate capability.

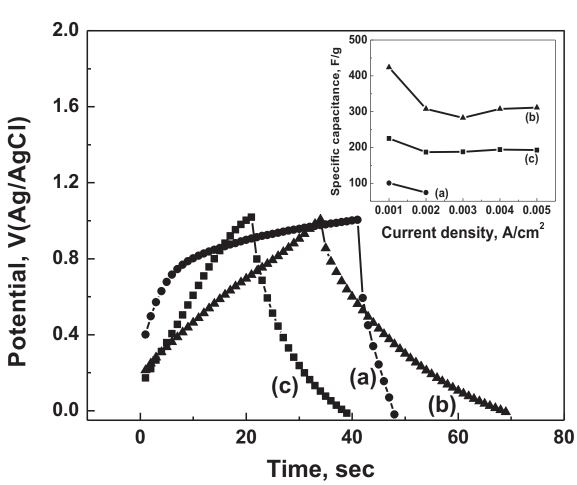

Fig. 8. Charge–discharge profiles for CH-free MnO_2 film (a) and MnO_2–CH hybrid nanocomposite films with low (b) and high (c) chitosan's M_w at a current density of 1 mA cm^{-2} in 0.5 M Na_2SO_4 electrolyte. The inset presents the variation of the discharge SC for the films with the discharge current density.

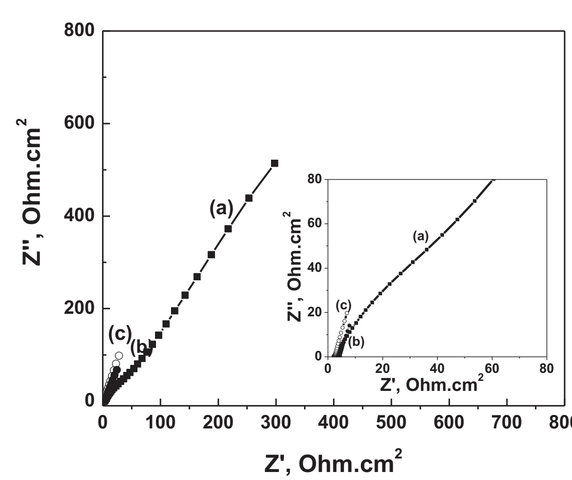

Fig. 9. Nyquist plots for CH-free MnO_2 film (a) and MnO2–CH hybrid nanocomposite films with low (b) and high (c) chitosan's M_w investigated in 0.5 M Na_2SO_4 electrolyte. The inset is the high-frequency region of the recorded full impedance plots.

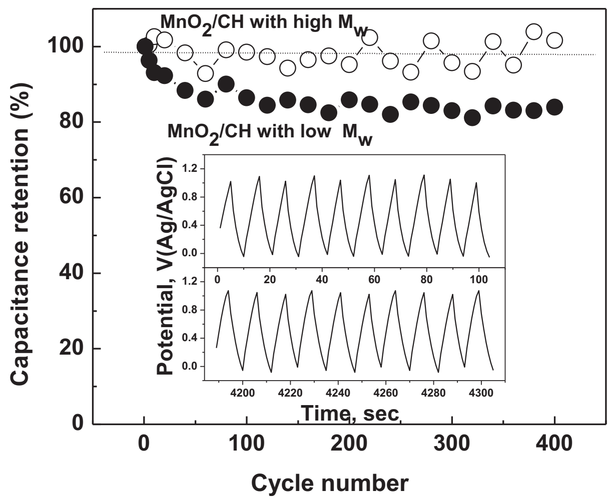

Fig. 10. Life-cycle data for the MnO_2–CH with high chitosan's M_w and MnO_2–CH with low chitosan's M_w films at current density of 3 mA cm^{-2}. The inset represents the first and last ten charge–discharge cycles for the MnO_2–CH film with high chitosan's M_w.

4. Conclusions

Chitosan provides a versatile means for assembling the amorphous MnO_2 nanoparticles into macro-scale components via one-step cathodic electrodeposition. The developed MnO_2–CH hybrid composite films present high SC, long cycle life and superior rate capability, making it promising ECs. The average discharge SC values for CH-free MnO_2, MnO_2–CH (high M_w) and MnO_2–CH (low M_w) films at a current density of 1 mA $cm^{-2}$are 100, 225 and 424 F g^{-1}, respectively. The presence of CH with its inherent binding properties allows the formation of adherent and crack-free deposits. In addition to that, CH presence not only efficiently promotes both ion and electron transport in the matrix of MnO_2 but also its structure feature. Most importantly, the developed new synthetic concept and the obtained novel structures are envisaged to pave the way toward a design and fabrication of analogous materials with enhanced properties for bio-fields and/or other applications.

Acknowledgments

The authors gratefully acknowledge the Missions Sector-Higher Education Ministry, Egypt for financial support through this work, Materials Science and Engineering Department at E-JUST.

References

[1] B.E. Conway, Electrochemical Supercapacitors: Scientific Fundamentals and Technological Applications, Plenum Press, New York [u.a.], 1999.
[2] R.F. Service, Science 313 (2006) 902.
[3] P. Simon, Y. Gogotsi, Nature Materials 7 (2008) 845–854.
[4] J.P. Zheng, T.R. Jow, Journal of the Electrochemical Society 142 (1995) L6–L8.
[5] P. Soudan, J. Gaudet, D. Guay, D. Bélanger, R. Schulz, Chemistry of Materials 14 (2002) 1210–1215.
[6] B.E. Conway, V. Birss, J. Wojtowicz, Journal of Power Sources 66 (1997) 1–14.
[7] P.A. Nelson, J.R. Owen, Journal of the Electrochemical Society 150 (2003) A1313–A1317.
[8] C. Lin, J.A. Ritter, B.N. Popov, Journal of the Electrochemical Society 145 (1998) 4097–4103.
[9] N.-L. Wu, S.-Y. Wang, C.-Y. Han, D.-S. Wu, L.-R. Shiue, Journal of Power Sources 113 (2003) 173–178.
[10] N.-L. Wu, Materials Chemistry and Physics 75 (2002) 6–11.
[11] T. Brousse, D. Bélanger, Electrochemical and Solid-State Letters 6 (2003) A244–A248.
[12] T. Brousse, M. Toupin, D. Bélanger, Journal of the Electrochemical Society 151 (2004) A614–A622.
[13] H.Y. Lee, J.B. Goodenough, Journal of Solid State Chemistry 144 (1999) 220–223.
[14] H.Y. Lee, V. Manivannan, J.B. Goodenough, Comptes Rendus de l'Académie des Sciences – Series IIC – Chemistry 2 (1999) 565–577.
[15] M. Toupin, T. Brousse, D. Bélanger, Chemistry of Materials 16 (2004) 3184–3190.
[16] S.C. Pang, M.A. Anderson, T.W. Chapman, Journal of the Electrochemical Society 147 (2000) 444–450.
[17] A.A. El-Moneim, M.M. Baker, International Journal of Electrochemical Science 7 (2012) 671–685.
[18] A.A. El-Moneim, International Journal of Hydrogen Energy 36 (2011) 13398–13406.
[19] A.A. El-Moneim, J. Bhattarai, Z. Kato, K. Izumiya, N. Kumagai, K. Hashimoto, ECS Transactions 25 (2010) 127–137.
[20] A.A. El-Moneim, K. Kumagai, K. Hashimoto, Materials Transactions 66 (2009) 1969–1977.
[21] A.A. El-Moneim, N. Kumagai, K. Asami, K. Hashimoto, Materials Transactions 46 (2005) 309–316.
[22] K. Hashimoto, H. Shinomiya, A. Nakazawa, Z. Kato, A.A. El-Moneim, Y. Niizeki, K. Asami, ECS Transactions 1 (2006) 49–59.
[23] S. Hassan, M. Suzuki, A. Abd El-Moneim, American Journal of Materials Science 2 (2012) 11–14.
[24] S. Hassan, M. Suzuki, A. Abd El-Moneim, Electrical and Electronic Engineering 2 (2012) 18–22.
[25] W. Wei, X. Cui, W. Chen, D.G. Ivey, Chemical Society Reviews 40 (2011) 1697–1721.
[26] G.F. Payne, S.R. Raghavan, Soft Matter 3 (2007) 521–527.
[27] E.P. Kuncoro, J. Roussy, E. Guibal, Separation Science and Technology 40, Marcel Dekker, New York, 2005, pp. 659–684.
[28] I.M.N. Vold, K.M. Vårum, E. Guibal, O. Smidsrød, Carbohydrate Polymers 54 (2003) 471–477.
[29] C.L. Schauer, M.-S. Chen, M. Chatterley, K. Eisemann, E.R. Welsh, R.R. Price, P.E. Schoen, F.S. Ligler, Thin Solid Films 434 (2003) 250–257.
[30] C.L. Schauer, M.-S. Chen, R.R. Price, P.E. Schoen, F.S. Ligler, Environmental Science & Technology 38 (2004) 4409–4413.
[31] E. Guibal, Separation and Purification Technology 38 (2004) 43–74.
[32] S.R. Ahmed, A.B. Kelly, T.A. Barbari, Journal of Membrane Science 280 (2006) 553–559.
[33] Z.-Y. Deng, J. She, Y. Inagaki, J.-F. Yang, T. Ohji, Y. Tanaka, Journal of the European Ceramic Society 24 (2004) 2055–2059.
[34] A. Kaushik, R. Khan, P.R. Solanki, P. Pandey, J. Alam, S. Ahmad, B.D. Malhotra, Biosensors and Bioelectronics 24 (2008) 676–683.
[35] F. Tian, Y. Liu, K. Hu, B. Zhao, Carbohydrate Polymers 57 (2004) 31–37.
[36] S. Karuppuchamy, J.M. Jeong, Journal of Oleo Science 55 (2006) 263–266.
[37] M. Ocaña, Colloid & Polymer Science 278 (2000) 443–449.
[38] C.M. Julien, M. Massot, C. Poinsignon, Spectrochimica Acta Part A: Molecular and Biomolecular Spectroscopy 60 (2004) 689–700.
[39] Q. Lu, Y. Zhou, Journal of Power Sources 196 (2011) 4088–4094.
[40] A. Celzard, F. Collas, J.F. Marêché, G. Furdin, I. Rey, Journal of Power Sources 108 (2002) 153–162.
[41] T. Tüken, B. Yazıcı, M. Erbil, Progress in Organic Coatings 50 (2004) 115–122.
[42] M.D. Stoller, S. Park, Y. Zhu, J. An, R.S. Ruoff, Nano Letters 8 (2008) 3498–3502.